

# How to Train Your Dragon: Quantum Neural Networks

Hao Zhang<sup>1</sup> and Alex Kamenev<sup>1,2</sup>

<sup>1</sup>*School of Physics and Astronomy, University of Minnesota, Minneapolis, MN 55455, USA and*

<sup>2</sup>*William I. Fine Theoretical Physics Institute, University of Minnesota, Minneapolis, MN 55455, USA*

Training of neural networks (NNs) has emerged as a major consumer of both computational and energy resources. We demonstrate that quantum annealing platforms, such as D-Wave, can enable fast and efficient training of classical NNs, which are then deployable on conventional hardware. From a physics perspective, NN training can be viewed as a dynamical phase transition: the system evolves from an initial spin glass state to a highly ordered, trained state. This process involves eliminating numerous undesired minima in its energy landscape—akin to cutting off the ever-regenerating heads of a dragon. The advantage of annealing devices is their ability to rapidly find multiple deep states (dragon heads to be cut). We found that this quantum-assisted training achieves superior performance scaling compared to classical backpropagation methods, with a notably higher scaling exponent (1.01 vs. 0.78). It may be further increased up to a factor of 2 with a fully coherent quantum platform using a variant of the Grover algorithm. Furthermore, we argue that even a modestly sized annealer can be beneficial to train a deep NN by being applied sequentially to a few layers at a time.

## I. INTRODUCTION

Neural networks (NNs) [1–8] have become one of the most transformative technologies, accelerating progress across multiple fields. A key factor in the revival and success of neural networks[7–13] is the development of efficient training methods. Techniques such as stochastic gradient descent[14], backpropagation[15], pre-training[5], ReLU activation[16], residual connections[17] have paved the way for training deep NNs effectively, leading to groundbreaking applications, such as AI. Yet, this progress comes at extraordinary costs, as training state-of-the-art models now routinely requires massive computational and energy resources. Moreover, extrapolating current trends suggests even steeper future costs. This motivates the search for fundamentally new training paradigms.

Meanwhile, quantum technologies have achieved critical milestones in recent years[18–23]. Of particular interest are quantum annealers, analog quantum computing devices engineered to exploit quantum coherent evolution to explore energy landscapes[24–34]. The modern quantum annealing architecture is already approaching  $10^4$  qubits[32, 34], with demonstrated advantage in combinatorial optimizations[34–37] and quantum dynamics simulations [22, 32].

Several recent studies have explored the synergy between neural networks and quantum effects [38–50]. In this paper, we adopt a different perspective, which takes advantage of quantum annealers’ capability to rapidly map out low-energy landscapes of (e.g., classical) spin glass models. Here we show how one may take advantage of it to accelerate NNs training. Once trained, such NNs can be deployed on classical hardware, combining the advantages of quantum and classical computing.

The approach is based on the observation that the training process drives NNs through a phase transition from an initial glassy state to a highly ordered trained state [51, 52]. The quantum dynamics facilitates such

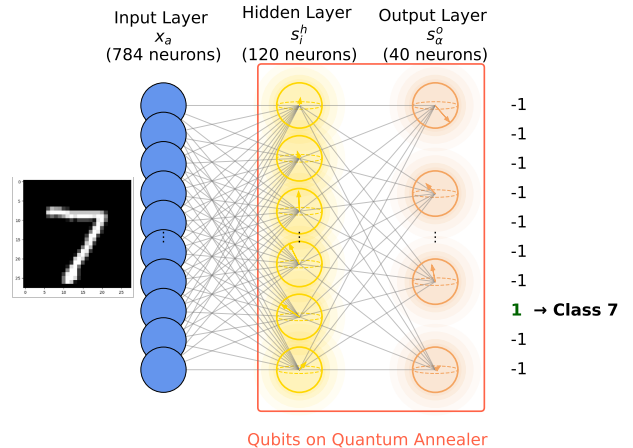


FIG. 1. NN architecture implemented on the D-Wave annealer. The input layer consists of 784 neurons, representing pixels of  $28 \times 28$  MNIST images. The hidden and output layers, comprised of 120 and 40 neurons respectively, are encoded as qubits on the quantum annealer. Each neuron in the output layer represents a digit class (0–9), with the 4-fold error-correcting redundancy. An output layer qubit, measured +1 indicates the digit class.

a transition due to its inherent ability to escape local minima[32, 37]. It thus allows one to efficiently explore the hierarchical basin structure of the low-energy landscape [37], which appears to be a key for accelerating NNs’ training. Being implemented on the D-Wave quantum annealer [31, 32], the quantum-assisted training algorithm demonstrates clear practical scaling advantages compared to classical training methods. Moreover, we show that a variant of Grover search algorithm [53], known as amplitude amplification protocol [54], implemented on a fully coherent quantum annealer, can further accelerate NNs’ training by potentially doubling the corresponding scaling exponent.

## II. NEURAL NETWORK TRAINING

Here we explain the principal idea behind NN training strategy amenable to be implemented on a quantum annealer. To be specific, consider a NN trained to recognize handwritten images of 0-9 digits. We adopted the architecture and image dataset (a subset of MNIST) as described in Ref.[49]. The network consists of three layers: one input layer, one hidden layer, and one output layer, see Fig. 1. The input layer contains  $784 = 28^2$  units, denoted by  $x_a$ , where  $0 \leq x_a \leq 1$  and  $a = 1, 2, \dots, 784$ , representing grayscale pixel values from handwritten images. The hidden layer consists of 120 units (implemented as qubits), denoted by  $s_i^h$ , where  $i = 1, 2, \dots, 120$  and  $h$  designates the hidden layer, taking values of  $\pm 1$  after a measurement of qubits'  $z$ -component. The output layer contains 40 units (also implemented as qubits), denoted by  $s_\alpha^o$ , here  $\alpha = 1, 2, \dots, 40$  and  $o$  stands for the output, also taking values of  $\pm 1$  upon  $z$ -measurement.

Connections from classical units in the input layer to quantum units in the hidden layer are implemented through local bias fields,  $h_i$ :

$$h_i[x] = \sum_{a=1}^{784} W_{ia} x_a, \quad (1)$$

where  $W_{ia}$  matrix represents coupling strengths between them. Quantum units in the hidden and output layers are connected through couplings  $J_{i\alpha}$  in the bare NN Hamiltonian,

$$H_0 = \sum_{i\alpha} J_{i\alpha} Z_i^h Z_\alpha^o + \sum_{i=1}^{120} b_i^h Z_i^h + \sum_{\alpha=1}^{40} b_\alpha^o Z_\alpha^o, \quad (2)$$

where  $Z_i^h, Z_\alpha^o$  are Pauli-Z matrices acting on qubits  $s_i^h$  and  $s_\alpha^o$  respectively, and  $b_i^h$  and  $b_\alpha^o$  are bias parameters. Note that there are no couplings within the same layer. Hamiltonian of NN with an input image,  $x$ , is given by:

$$H[x] = H_0 + \sum_{i=1}^{120} h_i[x] Z_i^h, \quad (3)$$

where the argument,  $[x]$ , emphasizes its dependence on an input training or test image,  $x$ .

When the neural network has already been trained, it works in the following way. An input image,  $x$ , to be inferred, is encoded into the bias fields,  $h_i[x]$ , as in Eq. (1). One looks then for a 160-spin configuration,  $\{s_i^h, s_\alpha^o\}$ , providing a ground (or a low-energy) state of the Hamiltonian  $H[x]$ . Specifically, the output part,  $s_\alpha^o$ , of the resulting ground state is used to predict the image class,  $\tilde{y} = 0, 1, \dots, 9$ . To this end the 40 output units are grouped into 10 groups by summing every four consecutive output values, forming a 10-component vector. A class predictor,  $\tilde{y}$ , is given by a position of the maximum component in this vector. This 4-fold redundancy of the output layer serves as a simple majority-rule error-correcting mechanism.

As explained below, the fully trained neural network spin-Hamiltonian,  $H[x]$ , is *not* a glass. Rather, its energy landscape contains a *single* (in case of the input image resembling one of training images) deep basin of attraction. Therefore, finding its ground state is a computationally easy task, which may be accomplished by, e.g., a simulated classical annealing. On the contrary, the training stage involves dealing with a glassy energy landscape. It can thus significantly benefit from using a quantum annealer, as explained below.

First we describe a training routine, known as *equilibrium propagation* [55], which will be subsequently modified to take advantage of quantum capabilities. To train the NN, it introduces the *nudge* Hamiltonian,  $H_N[x, y]$ , which depends on a training image,  $x$ , and its apriori known class  $y = 0, 1, \dots, 9$ , as

$$H_N[x, y] = H[x] - \sum_{\alpha=1}^{40} n_\alpha[y] Z_\alpha^o, \quad (4)$$

where  $n_\alpha[y]$  is a nudge bias encoding the class,  $y$ , of each training image,  $x$ , as  $n_\alpha[y] = 1$  for  $4y < \alpha \leq 4(y+1)$ , and  $n_\alpha[y] = -1$  otherwise.

The training process involves multiple updates of the network parameters. Initially, all parameters  $W_{ia}, J_{i\alpha}, b_i^h, b_\alpha^o$  are chosen randomly [56]. In each update step, a training image,  $x$ , belonging to a class  $y$ , is randomly selected from the dataset. One then looks for two low-energy states: the first,  $\{s_i^h, s_\alpha^o\}$ , of the system Hamiltonian  $H[x]$ , and the second,  $\{s_i^{h,N}, s_\alpha^{o,N}\}$ , of the nudge Hamiltonian  $H_N[x, y]$  [57]. The parameters are updated based on the differences between these two states. Minimization of the loss function leads to the following update rules [55]:

$$\Delta W_{ia} = \delta_W (s_i^h x_a - s_i^{h,N} x_a), \quad (5a)$$

$$\Delta J_{i\alpha} = \delta_J (s_i^h s_\alpha^o - s_i^{h,N} s_\alpha^{o,N}), \quad (5b)$$

$$\Delta b_i^h = \delta_h (s_i^h - s_i^{h,N}), \quad (5c)$$

$$\Delta b_\alpha^o = \delta_o (s_\alpha^o - s_\alpha^{o,N}), \quad (5d)$$

where  $\delta_W, \delta_J, \delta_h$ , and  $\delta_o$  are small positive learning rates.

If the low-energy state sampled from  $H[x]$  is identical (or very close) to that from  $H_N[x, y]$ , it implies that the network already produces the correct output. In this case the parameter do not update. However, if the state from  $H[x]$  differs from the one sampled from  $H_N[x, y]$ , the update rules penalize this difference by increasing the energy of this incorrect state. As a result, the likelihood of sampling this state or its neighbors in the future trials decreases. Through repeated updates, the energy landscapes of  $H[x]$  and of  $H_N[x, y]$  gradually align. Since the latter is engineered to enforce the output layer units to predict the proper class,  $y$ , the former inherits the same trait, without having the nudge bias, Eq. (4), (not known apriori for test images). Once this is achieved, the neural network is considered to be trained. Presenting NN with

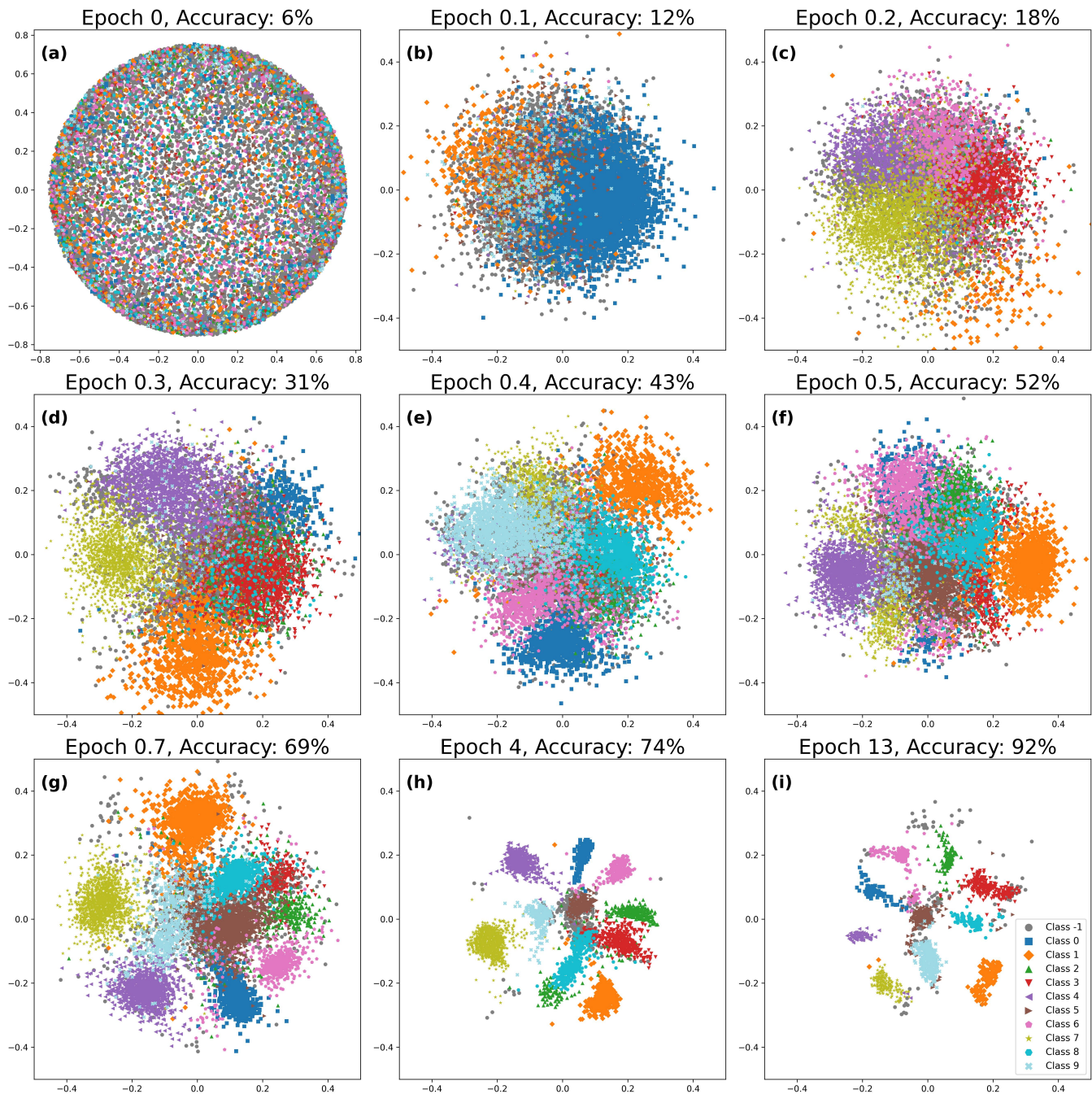


FIG. 2. Development of the NN visualized through low-energy states of  $H[x]$ , sampled by the D-Wave annealer. Each subplot corresponds to a different training epoch, with the test accuracy indicated. For each image in the test set (100 images total, 10 per class), 100 low-energy states were sampled using fixed network weights at a given epoch. These  $10^4$  states are projected from the 160-dimensional hypercube onto 2D using multidimensional scaling (MDS), preserving Hamming distances. Points are color-coded by their output class (0–9); gray points (class –1) indicate unclassified states. The late stages clearly demonstrate the appearance of dragon heads, with 9 of them needed to be cut off for any given training image,  $x$ .

all images from the training set along with corresponding adjustments of the parameters, Eq. (5), is called a training epoch. Number of such epochs needed to fully train NN may range from dozens to thousands.

### III. UNDERSTANDING NN TRAINING MECHANISM

To better understand how NN develops its ability to classify images, we utilized D-Wave’s quantum annealer

to sample low-energy states of (classical) Hamiltonians (3) and (4) using a quantum annealing protocol (specified below). We used a training set (1000 images, 100 per class) to train the NN for 13 epochs. At various stages of the training process we employed a test set (100 images total, 10 per class) to visualize the energy landscape of NN Hamiltonian, (3). To this end we sampled 100 low-energy states for each test image,  $x$ , 10,000 low-energy states in total. We then applied Multidimensional Scaling (MDS) using the scikit-learn library [58], projecting high-dimensional spin configurations (hypercube with dimensionality  $N = 160$ ) onto a two-dimensional plane. The MDS algorithm preserves the pairwise Hamming distances as closely as possible in the 2D representation.

Figure 2 shows the resulting 2D visualizations for 9 representative instances during the training history. Each point represents one of  $10^4$  low-energy states, color-coded by their output classes (0-9) (with gray points, labeled as class -1, indicating unclassified states in cases when the output vector does not have a single largest component). The evolution of the low-energy landscape illustrates the development of the NN from a random initialization stage toward a highly structured mature stage. As training progresses, the landscape develops 10 distinct well-separated low-energy basins, representing 10 classes. Correspondingly the NN's recognition accuracy on the test set increases from 6% to 92%. It can be further increased with a few extra training epochs.

Figure 3 gives a more detailed view of this process. The first row displays five examples of training images of the digit 7. Each image is fed into the NN and, as previously explained, low-energy states of the Hamiltonian  $H[x]$  with those images,  $x$ , belonging to the class  $y = 7$ , are sampled and plotted via the 2D MDS visualization. Dots are again color-coded according to their output class,  $\tilde{y}$ . Notice that the latter may or may not be equal to 7, representing correct or incorrect recognition respectively. The second and third rows display low-energy states for a poorly- and a well-trained NN. Each column corresponds to the same input image shown in the first row. In the poorly trained network (second row), one observes a mixed distribution of states associated with multiple output classes. As training progresses, the low-energy states become more closely spaced and their output class is almost surely  $\tilde{y} = 7$ .

The lesson is that the training process can be viewed as a phase transition from a glassy phase (no explicit structure) to an ordered phase (a single deep basin for any image,  $x$ ). (It is extremely important that images with distinct output classes produce such a deep basin in far-apart regions of the hypercube.) Such a transition makes the low energy states of the NN Hamiltonian loaded with an image,  $x$ , Eq. (3), to be concentrated within a narrow basin, having the same output class,  $\tilde{y} = y$ , where  $y$  is the class of the image  $x$ . It achieves this goal by energetically penalizing all states with  $\tilde{y} \neq y$ . The question is thus if and how a quantum annealer can accelerate such a training transition.

#### IV. TAKING ADVANTAGE OF QUANTUM DEVICES

The main advantage of quantum hardware is its ability to produce low-energy states (as low as 0.1% above the ground state energy [37]) of Ising-like Hamiltonians, extremely fast (eg., microseconds in case of D-Wave). Another useful feature is its ability to localize the search to specific parts of the hypercube. The latter capability is provided by the *cyclic annealing* protocol [34, 35, 37]. Unlike the more traditional forward annealing, it biases the search to a vicinity of a chosen (so-called *reference*) state.

The equilibrium training algorithm, described above, looks for a low-energy state,  $\{s_i^h, s_\alpha^o\}$ , which needs to be sufficiently far from the nudge state  $\{s_i^{h,N}, s_\alpha^{o,N}\}$ , to generate evolution of NN parameters according to Eq. (5). The quantum device can quickly produce  $m \gg 1$  states,  $\{s_i^{h,\gamma}, s_\alpha^{o,\gamma}\}$ , where  $\gamma = 1, 2, \dots, m$ . Moreover, they may be engineered to be away from the nudge state by the choice of initial reference states of the cyclic annealing protocol. One can then penalize against all such wrong states simultaneously by substituting

$$\begin{aligned} s_i^h &\rightarrow \frac{1}{m} \sum_{\gamma=1}^m s_i^{h,\gamma}, & s_\alpha^o &\rightarrow \frac{1}{m} \sum_{\gamma=1}^m s_\alpha^{o,\gamma}, \\ s_i^h s_\alpha^o &\rightarrow \frac{1}{m} \sum_{\gamma=1}^m s_i^{h,\gamma} s_\alpha^{o,\gamma} \end{aligned} \quad (6)$$

in Eq. (5). We call the training routine given by Eqs. (5)-(6) – the *dragon training*, because it allows one to cut multiple heads of the dragon (i.e. penalize all wrong basins) with a single swing of a sword (i.e. single update of the NN parameters).

In fact, Fig. 2 shows exactly where are those dragon heads to be cut. They are in the 9 basins with wrong output classes,  $\tilde{y} \neq y$ . Indeed, Fig.4 illustrates how performance improves as the number of sampled states,  $m$ , increases during a fixed training epoch. All model parameters are initialized identically for each data point. A significant decrease in error rate is observed for  $m \lesssim 10$  and plateaus for larger  $m$ . To further optimize the training one should therefore look for  $m = 9$  dragon heads (low-energy states) within wrong basins. To this end one should initialize cyclic annealing from the reference states which are the nudge states of the 9 wrong basins. The latter are given by

$$s_\alpha^{o,\gamma} = n_\alpha[\tilde{y}^\gamma]; \quad s_i^{h,\gamma} = -\text{sign} \left( \sum_\alpha J_{i\alpha} n_\alpha[\tilde{y}^\gamma] + b_i^h + h_i[x] \right), \quad (7)$$

where  $x$  is the currently presented image with the class  $y$  and  $\tilde{y}^\gamma \neq y$  are 9 wrong output classes,  $\gamma = 1, \dots, 9$ .

We benchmark the dragon training against classical backpropagation. To ensure fairness, both methods employ identical neural network architectures and best-

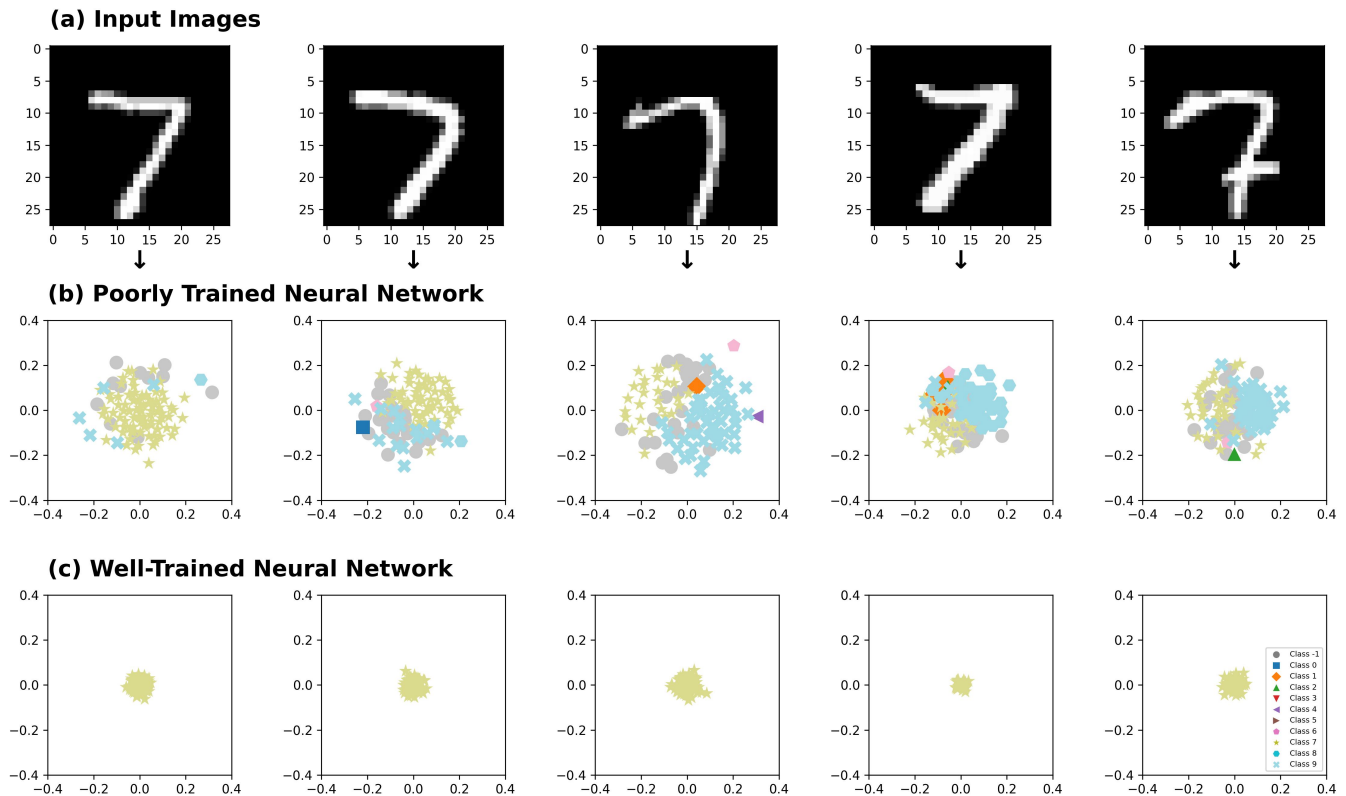


FIG. 3. Training NN to recognize digit 7. (a) Five representative  $28 \times 28$  test images of digit 7. (b) Corresponding low-energy states sampled from a poorly trained network’s energy landscape. Points are color-coded by their inferred output class ( $\hat{y}$ ), showing a scattered distribution across several classes. (c) Same test on a well-trained network exhibits tight clustering and uniform output labels ( $\hat{y} = 7$ ), showing that NN has developed a distinct energy basin for the digit 7.

practice settings. Classical training uses real-valued hidden and output units and ReLU activations in the hidden layer. Figure 5 shows the training error rate (1-accuracy) as a function of a number of training epochs in the log-log plot. It exhibits an algebraic relation,

$$\text{error rate} \propto (\# \text{ of epoch})^{-z}, \quad (8)$$

where  $z$  is the scaling exponent indicating training efficiency. Blue triangles are data from the equilibrium propagation training, Eq. (5), the corresponding exponent is  $z = 0.64$ . This is slightly worse than the conventional backpropagation technique (green squares,  $z = 0.78$ ). Red dots represent dragon training ( $m = 20$ ), exponent  $z = 1.01$ . The significantly larger exponent  $z = 1.01$  for the quantum technique indicates superior performance and efficiency compared to both backpropagation and equilibrium propagation. Importantly, the scaling exponent  $z$  serves as a more meaningful performance metric than the raw accuracy alone, as it is unaffected by the computational overhead per parameter update. For a typical number of epochs (100 to 500), a conventional NN training process would require 3 to 4 times the resources to match quantum dragon performance [59].

## V. QUANTUM COHERENT TRAINING

Equation (6) reminds an expectation value of corresponding  $Z^{h,o}$  operators in a many-body quantum state  $|\psi\rangle$ , which is a coherent superposition of  $m$  bit-string product states. Indeed, if

$$|\psi\rangle = \frac{1}{\sqrt{m}} \sum_{\gamma=1}^m |s_i^{h,\gamma}, s_\alpha^{o,\gamma}\rangle, \quad (9)$$

then Eq. (6) takes the form

$$s_i^h \rightarrow \langle \psi | Z_i^h | \psi \rangle, \quad s_\alpha^o \rightarrow \langle \psi | Z_\alpha^o | \psi \rangle, \quad s_i^h s_\alpha^o \rightarrow \langle \psi | Z_i^h Z_\alpha^o | \psi \rangle. \quad (10)$$

On the first glance this does not provide any advantage, since to calculate the expectation values, one should run an annealing protocol multiple times and perform measurements of the corresponding  $z$ -components. This is exactly what Eq. (6) prescribes to begin with. Yet, there may be a significant benefit hidden here as explained below.

Consider a state  $|\psi\rangle$ , reached upon a completion of a quantum annealing run, given by  $|\psi\rangle = U_{\text{QA}}[x]|\psi(0)\rangle$ , where an initial state,  $|\psi(0)\rangle$ , may be, eg., the  $x$ -polarized

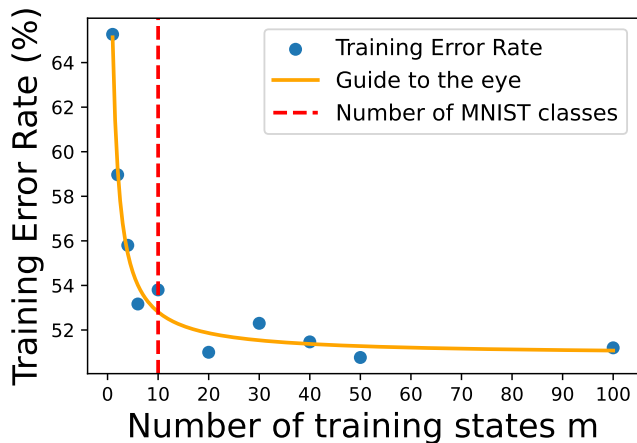


FIG. 4. Performance of dragon training during the first epoch: training error rate vs. number of training states  $m$ . The vertical red dashed line marks  $m_0 = 10$  – the number of MNIST classes. Notable improvement in accuracy is observed when  $m \lesssim m_0$ . Saturation behavior beyond this point suggests formation of  $m_0$  class-labeled basins in the low-energy space.

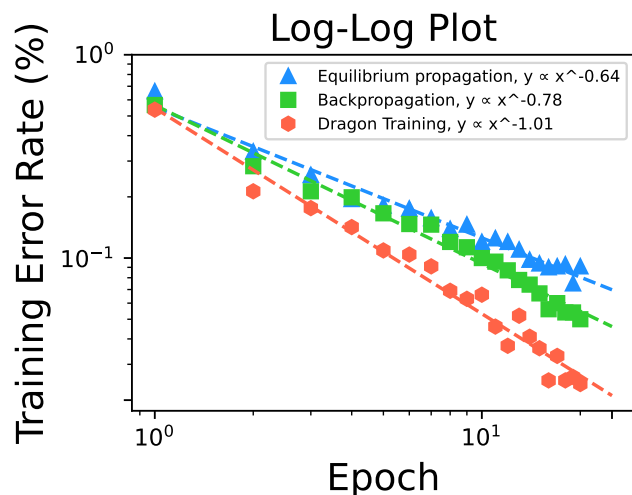


FIG. 5. Performance comparison of training methods on a log-log scale. D-Wave dragon training ( $m = 20$ , red hexagons,  $z = 1.01$ ) exhibits advantages scaling performance compared to backpropagation (green squares,  $z = 0.78$ ) and equilibrium propagation (also D-Wave) ( $m = 1$ , blue triangles,  $z = 0.64$ ).

product state,  $|\psi(0)\rangle = \prod_{i,\alpha} |+_i, +_\alpha\rangle$ . Here  $U_{\text{QA}}[x]$  is a unitary quantum evolution operator describing forward annealing with the time-dependent Hamiltonian:

$$H_{\text{QA}}(t) = (1-s(t)) \sum_{j(\alpha)} X_{j(\alpha)}^{h(o)} + s(t) H[x], \quad 0 \leq t \leq t_f, \quad (11)$$

where  $X_{j(\alpha)}^{h(o)}$  are Pauli- $X$ 's acting on all qubits,  $s(0) = 0$ , while  $s(t_f) = 1$ . The final state,  $|\psi\rangle = |\psi(t_f)\rangle$ , is a

superposition of the two orthogonal components

$$|\psi\rangle = A_y |\psi_y\rangle + A_{\tilde{y}} |\psi_{\tilde{y}}\rangle, \quad (12)$$

where state  $|\psi_y\rangle$  has output qubits pointing to the correct class,  $y$ , of the presented image,  $x$ , and state  $|\psi_{\tilde{y}}\rangle$  has output qubits pointing to all 9 incorrect classes,  $\tilde{y} \neq y$ . The corresponding amplitudes satisfy  $|A_y|^2 + |A_{\tilde{y}}|^2 = 1$ .

The goal of the training process is to make  $|A_{\tilde{y}}|$  as small as possible. As a result, during advanced training epochs  $|A_{\tilde{y}}| \ll 1$ . This is a good news for operating NN, but is a very bad news for it's further training. Indeed, the “correct” component,  $|\psi_y\rangle$ , is identical (or very close) to the ground state,  $|s_i^{h,N}, s_\alpha^{o,N}\rangle$ , of the nudge Hamiltonian. As a result, it does not lead to any improvement of NN parameters, see Eq. (5). It is thus the “wrong” component,  $|\psi_{\tilde{y}}\rangle$ , measured with the probability  $|A_{\tilde{y}}|^2 \ll 1$ , which contains all the information about dragon heads (basins) to be cut off. Therefore the training process may be significantly accelerated if one can use  $|\psi_{\tilde{y}}\rangle$  component, instead of  $|\psi\rangle$  in Eqs. (10) and (5) [60].

Notably, this can be achieved with the *amplitude amplification* procedure [54, 61–63], a generalization of the Grover search algorithm [53], which generates a rotation

$$U_{\text{amp}} |\psi\rangle = |\psi_{\tilde{y}}\rangle. \quad (13)$$

Engineering such a rotation requires order  $|A_{\tilde{y}}|^{-1} \gg 1$  applications of  $U_{\text{QA}}[x]$  and  $U_{\text{QA}}^\dagger[x]$  operations, along with a control operation performed on ancilla coupled to the  $y$ -output qubits ( $U_{\text{QA}}^\dagger[x]$  operation is achieved by running the annealing in the reversed time direction,  $t \rightarrow t_f - t$  in Eq. (11)). This should be contrasted with the order  $|A_{\tilde{y}}|^{-2} \gg |A_{\tilde{y}}|^{-1}$  annealing runs, required by the straightforward application of Eqs. (10), (12) to observe the  $|\psi_{\tilde{y}}\rangle$  component.

As a result, the fully quantum coherent annealing protocol, which incorporates amplitude amplification [54], may significantly further accelerate the training. Namely, it can potentially double the scaling exponent,  $z$ , in Eq. (8). We have not yet implemented such fully coherent protocol, since the D-Wave device is not expected to maintain coherence over multiple forward and backward runs of the annealing protocol. A smaller version of NN may be tested on a trapped ion platform[62] which exhibits much longer coherence time.

## VI. TRAINING DEEP NEURAL NETWORKS

Finally we discuss a possibility of training deep NNs with  $L$  layers with a modest size quantum annealer. The neurons in neighboring layers  $l$  and  $l + 1$  are connected through couplings  $J_{i_l i_{l+1}}$  in the bare Hamiltonian of a deep NN,

$$H_0 = \sum_{l=1}^{L-1} \sum_{\{i_l, i_{l+1}\}} \left( J_{i_l i_{l+1}} Z_{i_l}^l Z_{i_{l+1}}^{l+1} + b_{i_l}^l Z_{i_l}^l \right) + \sum_{i_L} b_{i_L}^L Z_{i_L}^L, \quad (14)$$

where  $Z_{i_l}^l$  are Pauli- $Z$  matrices acting on qubits  $s_{i_l}^l$  in layer  $l$ , and  $b_{i_l}^l$  are bias parameters. The last layer,  $l = L$ , serves as the output layer. To train such deep NN, one looks again for two low-energy states  $\{s_{i_l}^l\}$  of the system Hamiltonian,  $H[x]$ , and  $\{s_{i_l}^{L,N}\}$  of the nudge Hamiltonian,  $H_N[x, y]$ .

Due to the limited size of quantum annealers, one employs an active-layer sweep procedure. It calls for freezing all qubits along their total  $z$ -fields, except those in two (or more, depending on the capacity of the annealer) active layers. Starting from randomly initialized parameters, on the forward pass one allows layers  $l = 1, 2$  to be unfrozen and uses the annealer to find their low-energy configuration. Next, with the updated values from layer  $l = 1$ , one freezes all layers except  $l = 2, 3$ , and repeat the annealing process for those two layers. Proceeding layer by layer, one sequentially update qubits up to the output layer  $L$ .

Then, the backward sweep is performed: first, one activates layers  $l = L, L - 1$  only, and samples their  $m$  low-energy states from  $H[x]$  and one from  $H_N[x, y]$ . These are used to update parameters in layers  $l = L, L - 1$  via dragon training rules (5), (6). One then activates layers  $l = L - 1, L - 2$  and repeats updating down to the layer  $l = 1$ . One full forward and backward pass constitutes a single update of the network parameters.

This way one only needs an annealer capable of accommodating two successive layer of a deep NN to take advantage of its ability to rapidly search for multiple low-energy states. This observation may allow already exist-

ing annealers to accelerate training of practical NNs.

## VII. CONCLUSIONS

We have shown that even a modest-size quantum annealer can significantly accelerate NNs' training. The dragon training routine, suggested and implemented here with the D-Wave platform, exhibits the scaling exponent which is larger than both the equilibrium and the classical backpropagation algorithms. Moreover, we argued that a fully coherent annealer may be used to further increase the exponent up to a factor of two. Finally we discussed a way of beneficially using a quantum annealer with a number of qubits significantly smaller than the total number of neurons.

## DATA AVAILABILITY

The data that supports the findings of this study is available from the corresponding author upon request.

## CODE AVAILABILITY

The code that supports the findings of this study is available from the corresponding author upon request.

## ACKNOWLEDGMENTS

We are grateful to M. Amin, V. Galitski, and A. King for useful discussions. This work was supported by the NSF grant DMR-2338819.

- 
- [1] McCulloch, W. S. & Pitts, W. A logical calculus of the ideas immanent in nervous activity. *The bulletin of mathematical biophysics* **5**, 115–133 (1943). <https://doi.org/10.1007/BF02478259>.
- [2] Rosenblatt, F. The perceptron: A probabilistic model for information storage and organization in the brain. *Psychological Review* **65**, 386–408 (1958).
- [3] Hopfield, J. J. Neural networks and physical systems with emergent collective computational abilities. *Proceedings of the national academy of sciences* **79**, 2554–2558 (1982). <https://www.pnas.org/doi/abs/10.1073/pnas.79.8.2554>.
- [4] Hinton, G. E., Sejnowski, T. J. & Ackley, D. H. *Boltzmann machines: Constraint satisfaction networks that learn* (Carnegie-Mellon University, Department of Computer Science Pittsburgh, PA, 1984). <http://www.cs.toronto.edu/~hinton/absps/bmtr.pdf>.
- [5] Hinton, G. E., Osindero, S. & Teh, Y.-W. A fast learning algorithm for deep belief nets. *Neural Computation* **18**, 1527–1554 (2006).
- [6] Bengio, Y., Lamblin, P., Popovici, D. & Larochelle, H. Greedy Layer-Wise Training of Deep Networks. In *Advances in Neural Information Processing Systems*, vol. 19 (MIT Press, 2006). [https://proceedings.neurips.cc/paper\\_files/paper/2006/hash/5da713a690c067105aeb2fae32403405-Abstract.html](https://proceedings.neurips.cc/paper_files/paper/2006/hash/5da713a690c067105aeb2fae32403405-Abstract.html).
- [7] Krizhevsky, A., Sutskever, I. & Hinton, G. E. ImageNet Classification with Deep Convolutional Neural Networks. In *Advances in Neural Information Processing Systems*, vol. 25 (Curran Associates, Inc., 2012). [https://proceedings.neurips.cc/paper\\_files/paper/2012/hash/c399862d3b9d6b76c8436e924a68c45b-Abstract.html](https://proceedings.neurips.cc/paper_files/paper/2012/hash/c399862d3b9d6b76c8436e924a68c45b-Abstract.html).
- [8] LeCun, Y., Bengio, Y. & Hinton, G. Deep learning. *Nature* **521**, 436–444 (2015). <https://www.nature.com/articles/nature14539>.
- [9] Goodfellow, I. J. *et al.* Generative Adversarial Networks (2014). <http://arxiv.org/abs/1406.2661>. ArXiv:1406.2661.
- [10] Silver, D. *et al.* Mastering the game of Go with deep neural networks and tree search. *Nature* **529**, 484–489 (2016). <https://www.nature.com/articles/nature16961>.
- [11] Vaswani, A. *et al.* Attention Is All You Need (2023). <http://arxiv.org/abs/1706.03762>. ArXiv:1706.03762.

- [12] Brown, T. *et al.* Language Models are Few-Shot Learners. In *Advances in Neural Information Processing Systems*, vol. 33, 1877–1901 (Curran Associates, Inc., 2020). [https://proceedings.neurips.cc/paper\\_files/paper/2020/hash/1457c0d6bfbcb4967418bfb8ac142f64a-Abstract.html](https://proceedings.neurips.cc/paper_files/paper/2020/hash/1457c0d6bfbcb4967418bfb8ac142f64a-Abstract.html).
- [13] OpenAI. GPT-4 Technical Report (2024). <http://arxiv.org/abs/2303.08774>. ArXiv:2303.08774.
- [14] Robbins, H. & Monro, S. A Stochastic Approximation Method. *The Annals of Mathematical Statistics* **22**, 400–407 (1951). <https://www.jstor.org/stable/2236626>.
- [15] Rumelhart, D. E., Hinton, G. E. & Williams, R. J. Learning representations by back-propagating errors. *Nature* **323**, 533–536 (1986). <https://www.nature.com/articles/323533a0>.
- [16] Glorot, X., Bordes, A. & Bengio, Y. Deep Sparse Rectifier Neural Networks. In *Proceedings of the Fourteenth International Conference on Artificial Intelligence and Statistics*, 315–323 (JMLR Workshop and Conference Proceedings, 2011). <https://proceedings.mlr.press/v15/glorot11a.html>.
- [17] He, K., Zhang, X., Ren, S. & Sun, J. Deep Residual Learning for Image Recognition (2015). <http://arxiv.org/abs/1512.03385>. ArXiv:1512.03385.
- [18] Kim, Y. *et al.* Evidence for the utility of quantum computing before fault tolerance. *Nature* **618**, 500–505 (2023). <https://www.nature.com/articles/s41586-023-06096-3>.
- [19] Bluvstein, D. *et al.* Logical quantum processor based on reconfigurable atom arrays. *Nature* **626**, 58–65 (2024). <https://www.nature.com/articles/s41586-023-06927-3>.
- [20] Google Quantum AI and Collaborators. Quantum error correction below the surface code threshold. *Nature* **638**, 920–926 (2025). <https://www.nature.com/articles/s41586-024-08449-y>.
- [21] Gao, D. *et al.* Establishing a New Benchmark in Quantum Computational Advantage with 105-qubit Zhongzhong 3.0 Processor. *Physical Review Letters* **134**, 090601 (2025). <https://link.aps.org/doi/10.1103/PhysRevLett.134.090601>.
- [22] King, A. D. *et al.* Beyond-classical computation in quantum simulation. *Science* **388**, 199–204 (2025). <https://www.science.org/doi/10.1126/science.ado6285>.
- [23] Aboumrاد, W. *et al.* Accelerating large-scale linear algebra using variational quantum imaginary time evolution (2025). <http://arxiv.org/abs/2503.13128>. ArXiv:2503.13128.
- [24] Kadowaki, T. & Nishimori, H. Quantum annealing in the transverse Ising model. *Physical Review E* **58**, 5355–5363 (1998). <https://ui.adsabs.harvard.edu/abs/1998PhRvE...58.5355K>.
- [25] Brooke, J., Bitko, D., Rosenbaum, T. F. & Aeppli, G. Quantum Annealing of a Disordered Magnet. *Science* **284**, 779 (1999). <https://ui.adsabs.harvard.edu/abs/1999Sci...284..779B>.
- [26] Farhi, E. *et al.* A Quantum Adiabatic Evolution Algorithm Applied to Random Instances of an NP-Complete Problem. *Science* **292**, 472–475 (2001). <https://www.science.org/doi/10.1126/science.1057726>.
- [27] Santoro, G. E., Martoňák, R., Tosatti, E. & Car, R. Theory of Quantum Annealing of an Ising Spin Glass. *Science* **295**, 2427–2430 (2002). <https://ui.adsabs.harvard.edu/abs/2002Sci...295.2427S>.
- [28] Johnson, M. W. *et al.* Quantum annealing with manufactured spins. *Nature* **473**, 194–198 (2011). <https://www.nature.com/articles/nature10012>.
- [29] Jiang, S., Britt, K. A., McCaskey, A. J., Humble, T. S. & Kais, S. Quantum Annealing for Prime Factorization. *Scientific Reports* **8**, 17667 (2018). <https://www.nature.com/articles/s41598-018-36058-z>.
- [30] Criado, J. C. & Spannowsky, M. Qade: Solving Differential Equations on Quantum Annealers (2022). <http://arxiv.org/abs/2204.03657>. ArXiv:2204.03657.
- [31] King, A. D. *et al.* Coherent quantum annealing in a programmable 2,000 qubit Ising chain. *Nature Physics* **18**, 1324–1328 (2022). <https://www.nature.com/articles/s41567-022-01741-6>.
- [32] King, A. D. *et al.* Quantum critical dynamics in a 5000-qubit programmable spin glass. *Nature* (2023). <http://arxiv.org/abs/2207.13800>. ArXiv:2207.13800.
- [33] Bernaschi, M., González-Adalid Pemartín, I., Martín-Mayor, V. & Parisi, G. The quantum transition of the two-dimensional Ising spin glass. *Nature* **631**, 749–754 (2024). v.
- [34] Zhang, H., Boothby, K. & Kamenev, A. Cyclic quantum annealing: searching for deep low-energy states in 5000-qubit spin glass. *Scientific Reports* **14**, 30784 (2024). <https://www.nature.com/articles/s41598-024-80761-z>.
- [35] Wang, H., Yeh, H.-C. & Kamenev, A. Many-body localization enables iterative quantum optimization. *Nature Communications* **13**, 5503 (2022). <https://www.nature.com/articles/s41467-022-33179-y>.
- [36] Bauza, H. M. & Lidar, D. A. Scaling Advantage in Approximate Optimization with Quantum Annealing (2024). <http://arxiv.org/abs/2401.07184>. ArXiv:2401.07184.
- [37] Zhang, H. & Kamenev, A. On Computational Complexity of 3D Ising Spin Glass: Lessons from D-Wave Annealer (2025). <http://arxiv.org/abs/2501.01107>. ArXiv:2501.01107.
- [38] Adachi, S. H. & Henderson, M. P. Application of Quantum Annealing to Training of Deep Neural Networks (2015). <http://arxiv.org/abs/1510.06356>. ArXiv:1510.06356.
- [39] Biamonte, J. *et al.* Quantum machine learning. *Nature* **549**, 195–202 (2017). <https://www.nature.com/articles/nature23474>.
- [40] McClean, J. R., Boixo, S., Smelyanskiy, V. N., Babbush, R. & Neven, H. Barren plateaus in quantum neural network training landscapes. *Nature Communications* **9**, 4812 (2018). <https://www.nature.com/articles/s41467-018-07090-4>.
- [41] Lloyd, S. & Weedbrook, C. Quantum Generative Adversarial Learning. *Physical Review Letters* **121**, 040502 (2018). <https://link.aps.org/doi/10.1103/PhysRevLett.121.040502>.
- [42] Amin, M. H., Andriyash, E., Rolfe, J., Kulchitsky, B. & Melko, R. Quantum Boltzmann Machine. *Physical Review X* **8**, 021050 (2018). <https://link.aps.org/doi/10.1103/PhysRevX.8.021050>.
- [43] Dendukuri, A. *et al.* Defining Quantum Neural Networks via Quantum Time Evolution (2020). <http://arxiv.org/abs/1905.10912>. 1905.10912.
- [44] Job, J. & Adachi, S. Systematic comparison of deep belief network training using quantum annealing vs. classical techniques (2020). <http://arxiv.org/abs/2009.00134>.

- ArXiv:2009.00134.
- [45] Dixit, V., Selvarajan, R., Alam, M. A., Humble, T. S. & Kais, S. Training Restricted Boltzmann Machines With a D-Wave Quantum Annealer. *Frontiers in Physics* **9** (2021). <https://www.frontiersin.org/journals/physics/articles/10.3389/fphy.2021.589626/full>. Publisher: Frontiers.
- [46] Higham, C. F. & Bedford, A. Quantum deep learning by sampling neural nets with a quantum annealer. *Scientific Reports* **13**, 3939 (2023). <https://www.nature.com/articles/s41598-023-30910-7>.
- [47] Xie, R. & Kamenev, A. Quantum Hopfield Model with Dilute Memories (2024). <http://arxiv.org/abs/2405.13240>. ArXiv:2405.13240.
- [48] Senokosov, A., Sedykh, A., Sagingalieva, A., Kyriacou, B. & Melnikov, A. Quantum machine learning for image classification. *Machine Learning: Science and Technology* **5**, 015040 (2024). <https://dx.doi.org/10.1088/2632-2153/ad2aef>.
- [49] Laydevant, J., Marković, D. & Grollier, J. Training an Ising machine with equilibrium propagation. *Nature Communications* **15**, 3671 (2024). <https://www.nature.com/articles/s41467-024-46879-4>.
- [50] Barney, R., Lakhdar-Hamina, D. & Galitski, V. Natural Quantization of Neural Networks (2025). <http://arxiv.org/abs/2503.15482>. ArXiv:2503.15482.
- [51] Huang, H. *Statistical Mechanics of Neural Networks* (Springer Nature Singapore, Singapore, 2021). <https://link.springer.com/10.1007/978-981-16-7570-6>.
- [52] Barney, R., Winer, M. & Galitski, V. Neural Networks as Spin Models: From Glass to Hidden Order Through Training (2024). <http://arxiv.org/abs/2408.06421>. ArXiv:2408.06421.
- [53] Grover, L. K. A fast quantum mechanical algorithm for database search (1996). <http://arxiv.org/abs/quant-ph/9605043>. quant-ph/9605043.
- [54] Brassard, G., Hoyer, P., Mosca, M. & Tapp, A. Quantum Amplitude Amplification and Estimation. *Quantum Computation and Quantum Information, AMS Contemporary Mathematics, 305:53-74, 2002* **305**, 53–74 (2002). <http://arxiv.org/abs/quant-ph/0005055>.
- quant-ph/0005055.
- [55] Scellier, B. & Bengio, Y. Equilibrium Propagation: Bridging the Gap between Energy-Based Models and Backpropagation. *Frontiers in Computational Neuroscience* **11** (2017). <https://www.frontiersin.org/journals/computational-neuroscience/articles/10.3389/fncom.2017.00024/full>.
- [56] In our implementation,  $W_{i\alpha}$  is drawn from a uniform distribution over  $[-1/\sqrt{784}, 1/\sqrt{784}]$ ;  $J_{i\alpha}$  is drawn from a uniform distribution over  $[-1/\sqrt{120}, 1/\sqrt{120}]$ . The biases  $b_i^h, b_\alpha^o$  are initialized to zero.
- [57] The second step may be circumvented, as the strong nudge fixes  $s_\alpha^{o,N} = n_\alpha[y]$ , while  $s_\alpha^{o,h}$  is then simply determined by the sign of the local field as in Eq. (7).
- [58] Pedregosa, F. *et al.* Scikit-learn: Machine learning in Python. *Journal of Machine Learning Research* **12**, 2825–2830 (2011).
- [59] Additional testing under varied classical conditions did not match quantum basin training’s efficiency. Specifically, switching to sigmoid activations reduces  $z$  to 0.56, and increasing hidden units tenfold (from 120 to 1200 units) only marginally improves  $z$  to 0.84.
- [60] The cyclic annealing with reference states, Eq. (7), is not efficient in late epochs, since the basin, defined by the correct class,  $y$ , is so much attractive that almost every cycle ends up in it, even if the initial reference state is chosen in a basin with  $\tilde{y} \neq y$ .
- [61] Yan, B. *et al.* Fixed-point oblivious quantum amplitude-amplification algorithm. *Scientific Reports* **12**, 14339 (2022). <https://www.nature.com/articles/s41598-022-15093-x>.
- [62] Kikuchi, Y., Mc Keever, C., Coopmans, L., Lubasch, M. & Benedetti, M. Realization of quantum signal processing on a noisy quantum computer. *npj Quantum Information* **9**, 1–12 (2023). <https://www.nature.com/articles/s41534-023-00762-0>.
- [63] V, K. & Santhanam, M. S. Amplitude amplification and estimation using the atom-optics kicked rotor. *Physical Review A* **111**, 032601 (2025). <https://link.aps.org/doi/10.1103/PhysRevA.111.032601>.